



HAL
open science

Spectral decomposition unlocks ascidian morphogenesis

Joel Dokmegang, Emmanuel Faure, Patrick Lemaire, Ed Munro, Madhav Mani

► **To cite this version:**

Joel Dokmegang, Emmanuel Faure, Patrick Lemaire, Ed Munro, Madhav Mani. Spectral decomposition unlocks ascidian morphogenesis. *eLife*, 2024, 13, pp.RP94391. 10.7554/eLife.94391.1 . hal-04804074

HAL Id: hal-04804074

<https://hal.science/hal-04804074v1>

Submitted on 26 Nov 2024

HAL is a multi-disciplinary open access archive for the deposit and dissemination of scientific research documents, whether they are published or not. The documents may come from teaching and research institutions in France or abroad, or from public or private research centers.

L'archive ouverte pluridisciplinaire **HAL**, est destinée au dépôt et à la diffusion de documents scientifiques de niveau recherche, publiés ou non, émanant des établissements d'enseignement et de recherche français ou étrangers, des laboratoires publics ou privés.



Distributed under a Creative Commons Attribution 4.0 International License

1 Spectral decomposition unlocks 2 ascidian morphogenesis

3 **Joel Dokmegang**^{1,2*}, **Emmanuel Faure**^{4,6}, **Patrick Lemaire**^{4,5}, **Ed Munro**^{3†¶}, **Madhav**
4 **Mani**^{1,2*}

*For correspondence:

jdokmegang@gmail.com (NU);
madhav.mani@gmail.com (NU)

5 ¹Northwestern University; ²NSF-Simons Center for Quantitative Biology; ³University of
6 Chicago; ⁴University of Montpellier; ⁵CNRS; ⁶LIRMM

8 **Abstract** Describing morphogenesis generally consists in aggregating the multiple high
9 resolution spatiotemporal processes involved into reproducible low dimensional morphological
10 processes consistent across individuals of the same species or group. In order to achieve this
11 goal, biologists often have to submit movies issued from live imaging of developing embryos
12 either to a qualitative analysis or to basic statistical analysis. These approaches, however, present
13 noticeable drawbacks, as they can be time consuming, hence unfit for scale, and often lack
14 standardisation and a firm foundation. In this work, we leverage the power of a continuum
15 mechanics approach and flexibility of spectral decompositions to propose a standardised
16 framework for automatic detection and timing of morphological processes. First, we quantify
17 whole-embryo scale shape changes in developing ascidian embryos by statistically estimating the
18 strain-rate tensor field of its time-evolving surface without the requirement of cellular
19 segmentation and tracking. We then apply to this data spectral decomposition in space using
20 spherical harmonics and in time using wavelets transforms. These transformations result in the
21 identification of the principal dynamical modes of ascidian embryogenesis and the automatic
22 unveiling of its blueprint in the form of spectrograms that tell the story of development in ascidian
23 embryos.

25 Introduction

26 Morphogenesis, the emergence of shape in living systems, is a continuous process littered with
27 spatiotemporal dynamics at various timescales and lengthscales and significance. Developmental
28 biology aims at the identification, localisation, and timing of these processes. Once this work is car-
29 ried out in a given species, embryogenesis can then be described as a series of stages delineated
30 in space and time by the identified landmarks *Satoh (1978)*; *Nishida (1986)*; *Jeffery (1992)*; *Keller*
31 *et al. (2003)*; *Lemaire (2009)*; *Sherrard et al. (2010)*; *Hashimoto et al. (2015)*; *Hashimoto and Munro*
32 *(2018)*; *Guignard et al. (2020)*. In order to rigorously define development landmarks, biologists have
33 mostly had to submit imaged embryos either to qualitative analyses, or to rudimentary statistical
34 analysis. These methods however present major drawbacks. On the one hand, they can be time
35 consuming, hence unfit for scale. On the other hand, since morphogenetic processes tend to be
36 unique to a species, these simple methods often lack a general language and framework that per-
37 mit comparative analyses. For instance, whereas the analysis of cell counts can inform about the
38 proliferation dynamics in a tissue, it does not reveal anything about the shape of the system. For
39 this purpose, other measurements such as length, width, height, aspect ratios or curvatures would
40 be more suitable. Although efforts have been made to automate the staging of development in
41 living systems *Jones et al. (2022)*, these methods still rely on preliminary examination using tradi-
42 tional methods.

43 A standardized method able to identify key milestones in development and lay out the blueprint
44 of morphogenesis in a given system is henceforth needed. Recent breakthroughs in microscopy
45 technology have propelled the resolution of live imaging data to the sub-cellular scale, allowing
46 for the uncovering of precise cell and tissue shape dynamics *Tassy et al. (2006)*; *Stelzer (2015)*;
47 *Power and Huisken (2017)*. These advances have created an unprecedented opportunity for the
48 leveraging of computational methods in the study of morphogenesis *Tassy et al. (2006)*; *Michelin*
49 *et al. (2015)*; *Stegmaier et al. (2016)*; *Leggio et al. (2019)*; *Guignard et al. (2020)*. The rigorous and
50 physically motivated framework of continuum mechanics accommodates itself well to the flow-
51 like dynamics of biological tissues *Humphrey (2003)*; *Ambrosi et al. (2011)*; *Blanchard et al. (2009)*;
52 *Humphrey (2013)*; *Streichan et al. (2018)*. Within this framework, strain-rate fields, which measure
53 the rate at which the shape of a system changes with time, are suited to characterise the dynamical
54 behaviour of the system. Moreover, mounting evidence have informed of the requirement for
55 embryo-wide approaches in the study of morphogenetic flows *Streichan et al. (2018)*; *Mitchell*
56 *et al. (2022)*. However, although the evaluation of such global fields across the spatial and temporal
57 domains spanned by a system of interest may reveal valuable insights into its dynamical workings
58 *Bar-Kochba et al. (2015)*; *Stout et al. (2016)*; *Patel et al. (2018)*, their sole determination might not
59 be sufficient for a holistic description of the behaviour of the system: there is a need for novel
60 methods to analyse them.

61 This is especially true when it comes to morphogenesis *Dalmaso et al. (2021)*; *Romeo et al.*
62 *(2021)*; *Mitchell and Cislo (2022)*. The processes involved in development are inherently multiscale,
63 both in the spatial and temporal domains, and may interact or overlap *Godard and Heisenberg*
64 *(2019)*; *Dokmegang et al. (2021)*; *Dokmegang (2022)*. As it is the case with several species *Godard*
65 *and Heisenberg (2019)*, ascidian gastrulation is a playground featuring important displays of cellu-
66 lar divisions and tissue mechanics, most notably endoderm invagination *Lemaire (2009)*. The local
67 behaviors captured by indicators such as the strain-rate field might therefore arise from a non-
68 trivial superposition of these dynamical modes, essentially making these measurements complex
69 to interpret without further analysis. Spectral decomposition, whereby a signal is broken down into
70 its canonical components, is well suited to the study of systems that exhibit multimodal behaviors
71 *Romeo et al. (2021)*; *Dalmaso et al. (2021)*. The benefits are at least two-folds: (i) individual con-
72 stituents may represent distinct dynamical processes, thereby enabling the decoupling of physical
73 processes entangled in the data; (ii) only a handful of components may significantly contribute to
74 the original function, resulting in a compressed, lower dimensional representation that capture
75 the main features of the studied process. The canonical components usually take the form of well
76 known families of functions whose linear combination can reconstitute the original field.

77 In this work, we take advantage of segmented cellular data to develop a generic computational
78 framework able to identify and delineate the main features of morphogenesis. Our method takes
79 as input precise segmentations of cellular geometries, although only the embryonic surface would
80 suffice, and outputs spatiotemporal spectrograms of ascidian development in the form of heatmaps
81 that highlight key developmental processes and stages of ascidian gastrulation. By virtue of a novel
82 meshing scheme derived from level-set methods, raw cell geometry data is first transformed into
83 a single time-evolving embryonic surface on which the strain-rate tensor field can be computed.
84 The accuracy of our inference of a strain-rate field relies on high-frequency temporal sampling,
85 characterised by small deformations of the embryonic surface between subsequent time points.
86 The morphomaps we present are a result of spectral analyses of the strain-rate fields, featuring
87 spherical harmonics decomposition in the spatial domain and wavelet decomposition in the tem-
88 poral domain. In summary, our method can identify and classify dynamical morphogenetic events.
89 In particular, we are able to identify and distinguish the morphogenetic modes of gastrulation and
90 neurulation phases in ascidian development, recover the characteristic two step sequence of en-
91 doderm invagination originally described using 3D analysis of cell shapes *Sherrard et al. (2010)*,
92 and capture patterns of cellular divisions in ascidian development *Nishida (1986)*. Moreover, our
93 method identifies a distinctive stage of ascidian gastrulation, 'blastophore closure', which follows

94 endoderm invagination and precedes neurulation.

95 Results

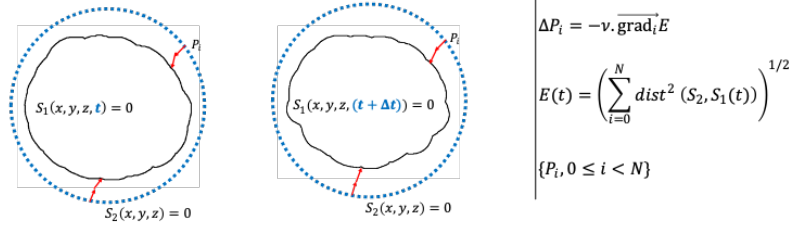
96 Definition of Lagrangian markers on the surface of the embryo

97 In order to recover a continuum description of the dynamics in ascidian morphogenesis, we aim to
98 examine the time evolution of strain-rate fields across the entire surface of developing embryos.
99 This endeavour however presents at least two significant challenges. On the one hand, strain-rate
100 computation requires the presence of fiducial markers on the surface of the embryo. Character-
101 istically, this requirement is not always accounted for in the imaging of developing embryos. On
102 the other hand, the outer layer of the embryo being constituted of single cell apical faces, even
103 if such markers had been defined at an earlier time point, uncontrolled stochastic biological pro-
104 cesses such as proliferation within the tissue might subsequently grossly uneven the distribution
105 of these markers, thus rendering the computed mechanical indicators at best imprecise. Given the
106 non-triviality of an experimental setup able to solve the described issues, a computational method
107 is required. The goal of such a method would be to computationally discretise an embryo surface
108 into a set of material particles whose trajectories can be tracked in small lapses of development.
109 The positions of these markers over time can then be used to derive mechanical indicators of de-
110 velopment dynamics *Humphrey (2003)*.

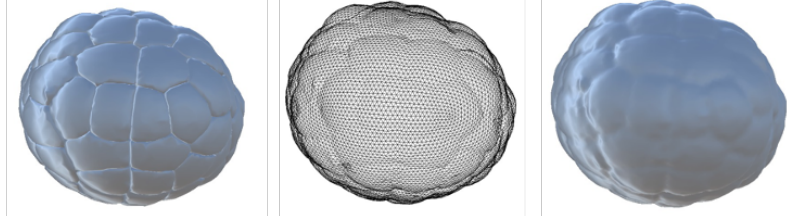
111 To achieve this fit, we first take advantage of the level set scheme described in *Zhao et al. (2000)*
112 to define static markers on the surface of the embryo at every timepoint of development. The gist
113 of our method resides in the definition of a homeomorphic map between the surface of the em-
114 bryo ($S_1(t)$) and a topologically equivalent mesh ($S_2(t)$) whose number of vertices, faces and edges
115 remain fixed (fig. 2a). Conformal parametrisations of embryonic shape have been used in other
116 systems *Alba et al. (2021)*. Here, the topologically equivalent mesh consists of a sphere resulting
117 from successive butterfly subdivisions of an icosahedron *Hardy and Steeb (2008)*. Using a homeo-
118 morphic map, this mesh can be deformed to match the surface of the embryo at each time point of
119 development (fig. 2b). As in *Zhao et al. (2000)*, the map is obtained by finding the positions of $S_2(t)$
120 vertices that minimize the distance between both surfaces (fig. 2a, right). At the initial time point,
121 $S_2(t)$ is chosen to be a sphere enclosing the embryo. For various reasons, including computational
122 efficiency, variants of this method can be defined such that, for instance, at subsequent time steps,
123 linear combinations of the sphere and its deformations matching the embryo at preceding steps
124 are used. Further details are given in the Methods section.

125 Next, via a numerical study, we assert that markers defined as such behave as Lagrangian parti-
126 cles in small increments of developmental dynamics. To support this point, we identify on the raw
127 dataset the positions of cellular junctions at the surface of the embryo and evaluate how well our
128 virtual markers mimic their movements in time. We measure the relative displacement between a
129 cellular junction (fig. 1c red points) and its corresponding vertex (fig. 1c, green points) at consecutive
130 time points. We take the difference between these distances and normalise it by the average side
131 length of cell apices. Despite gross approximations inherent to the nature of the dataset (geomet-
132 ric meshes) and the process of identifying cellular junctions (averaging the barycenters of closest
133 triangles between three or more cells in contact), the displacement between cellular junctions and
134 their markers remains on average relatively small (under 8%, fig. 1d). We further show that this
135 characteristic is independent of the number of particles used in the method (sup fig. 1c), making it
136 a remarkable property of the scheme. This result sheds even more favorable light on the method
137 when considering that cellular junctions, precisely because they are the meeting point of three or
138 more cells, are expected to exhibit more chaotic behaviour than single cell particles. Moreover,
139 these numbers are skewed by large scale morphogenesis processes such as synchronised cell di-
140 visions, as evidenced by spikes in fig. 1d, and fast-paced endoderm gastrulation, as highlighted by
141 higher errors at the vegetal pole of the embryo during this phase (red dots in fig. 1c, right).

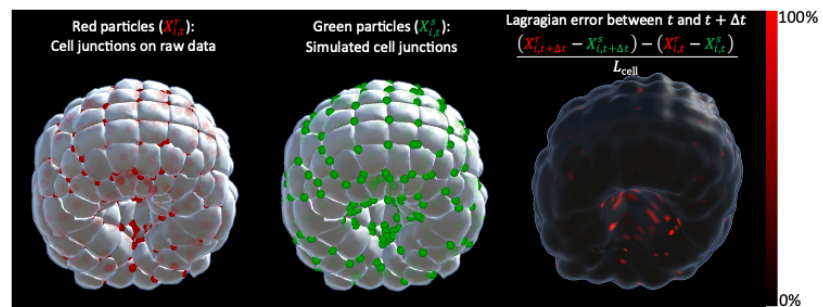
a. Level set scheme for evolving surface generation



b. Raw data, resulting mesh, rendered embryo surface



c. Method validation: Tracking cellular junctions



d. Relative displacement between cellular junctions and their markers over time

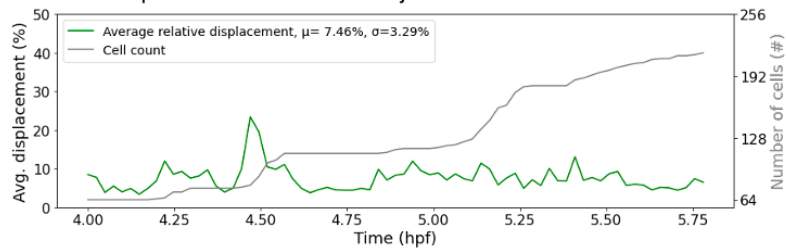


Figure 1. Level-sets inspired Lagrangian markers. **a)** *Left* Schematics of the level set method. *Right* Fundamentals of the numerical scheme that shapes S_2 into S_1 . **b)** *Left* Raw data consisting of geometric meshes of single cells spatially organised into the embryo. *Center* Embryo surface mesh resulting from the application of the level set scheme. *Right* Rendering of the embryonic surface. **c)** *Left* Identification of cellular junctions (*red dots*). *Center* Corresponding markers (*green dots*, defined as vertices on the computed embryonic surface closest to the junctions). *Right* Relative displacement between junctions and their markers at consecutive timepoints. **d)** Plot over time of the relative displacement between cellular junctions and their markers.

Strain rate Field describes ascidian morphogenesis

142
143
144
145
146
147
148
149
150

Once a mesh representing the surface has been constructed for the embryo surface, we proceed with the computation of the strain-rate fields across the surface of the embryo and throughout development timeline. Thanks to the Lagrangian nature of mesh vertices, a velocity field can be defined on the mesh. Although particles at every given time point live on the 2D surface of the embryo, their trajectories in time involve greater degrees of freedom in the 3D space. A correct parametrisation of the velocity field at every position henceforth requires three coordinates $\mathbf{v}(\mathbf{x}) = (v_x(\mathbf{x}), v_y(\mathbf{x}), v_z(\mathbf{x}))^T$. The strain rate field is derived as the symmetric part of the discrete gradient of the velocity field, computed as described in *Mancinelli et al. (2018)*. Intuitively, the strain rate

151 evaluated on a given mesh vertex measures how the velocity vector varies in the neighbourhood
152 this point *Mancinelli et al. (2018)*; *De Goes et al. (2020)*.

$$D(t, \mathbf{x}) = \text{sym}(\nabla \mathbf{v}(t, \mathbf{x})) \quad (1)$$

153 The mathematical construction of the strain rate eq. 1 implies that its algebraic representation
154 takes the form of a second order tensor which can be written down as a 3×3 matrix $(D)_{ij}$. The diag-
155 onal elements of this matrix capture the linear strain rate in the x, y, z axes, depicting the change
156 in length per unit length. The non-diagonal elements stand for shear strain rates in the the xy, xz
157 and yz directions. Because D is symmetric, there exists an alternative representation which holds
158 stronger local geometric meaning. This representation is obtained by computing the eigenvectors
159 and eigenvalues of the strain rate tensor. Eigenvectors in this sense stand for orthogonal spatial di-
160 rections that are not rotated, but only stretched, by the application of the strain rate matrix. They
161 define the principal axes of a coordinate system in which the strain rate tensor would be solely
162 composed of maximal linear strain rates (fig. 2a). From this decomposition, we derive a scalar field
163 that is computed at every mesh particle as the square root of the sum of the squared eigenval-
164 ues of the strain-rate (fig. 2b). Intuitively, this field describes the magnitude of the rate of change
165 underwent by a particle at the surface of the embryo in the three orthogonal spatial directions of
166 most significant rate of change.

167 In order to minimize undesirable artifacts that may arise from numerical inefficiencies, we ap-
168 ply a Gaussian filter to the strain rate tensor field before deriving the scalar field. At each particle
169 location, we apply a Gaussian convolution mask spanning its first and second order neighbour-
170 hood. A similar smoothing process is also used in the time domain. Interestingly, this strain-rate
171 derived scalar field remarkably mirrors well-known features of ascidian development. Similarities
172 between the spatiotemporal distribution of morphogenesis processes described in the literature
173 and heatmaps of this field on the evolving embryo surface emerge. On the one hand, wider spatial
174 gradients of yellow to red depicting higher morphological activity portray the spatiotemporal lo-
175 cations of endoderm invagination in the embryonic vegetal pole (fig. 2b, *center-left*), synchronised
176 rounds of division in the animal pole, and zippering in the neural plate *Hashimoto et al. (2015)*
177 (fig. 2b, *center-right, right*). On the other hand, known spatiotemporal locations of low morphologi-
178 cal significance in the embryo exhibit stronger concentration of mechanical activity on cell bound-
179 aries, with the corollary that cellular identities are mostly preserved (fig. 2b, $t = 4hpb$). A notable
180 by-product of this scalar field is the evidencing of the duality of the embryo as both a sum of parts
181 constituted of cells and an emerging entity in itself: the strain rate field clearly discriminates be-
182 tween spatiotemporal locations where isolated single cell behaviours are preponderant and those
183 where coordinated cell behaviours dominate.

184 This brief overview already demonstrates the riches in a quantitative, spatially global and not
185 event-driven approach to study morphogenesis. It also sets the stage for further analysis of mor-
186 phogenesis dynamics in the ascidian embryo.

187 **Spectral decomposition in space: Spherical harmonics reveal the main modes of** 188 **ascidian morphogenesis**

189 In order to capture relevant features of the strain rate field in the spatial domain, we conduct a
190 spectral analysis of the scalar strain rate field. The family of spherical harmonic functions stands
191 out as a de-facto standard for the study of signals defined on a unit sphere, and by extension on
192 surfaces homeomorphic to the sphere. Spherical harmonics form an infinite orthonormal basis of
193 functions defined on the surface of the sphere and represent a generalisation of the Fourier series
194 for functions of two variables *Knaack and Stenflo (2005)*. Unsurprisingly, these functions play an
195 important role in many branches of science including quantum mechanics and geophysics *Knaack*
196 *and Stenflo (2005)*; *Dahlen and Tromp (2021)*. Spherical harmonics have recently been used in
197 studies of morphogenesis in zebrafish and mouse *Romeo et al. (2021)*; *Dalmasso et al. (2021)*.

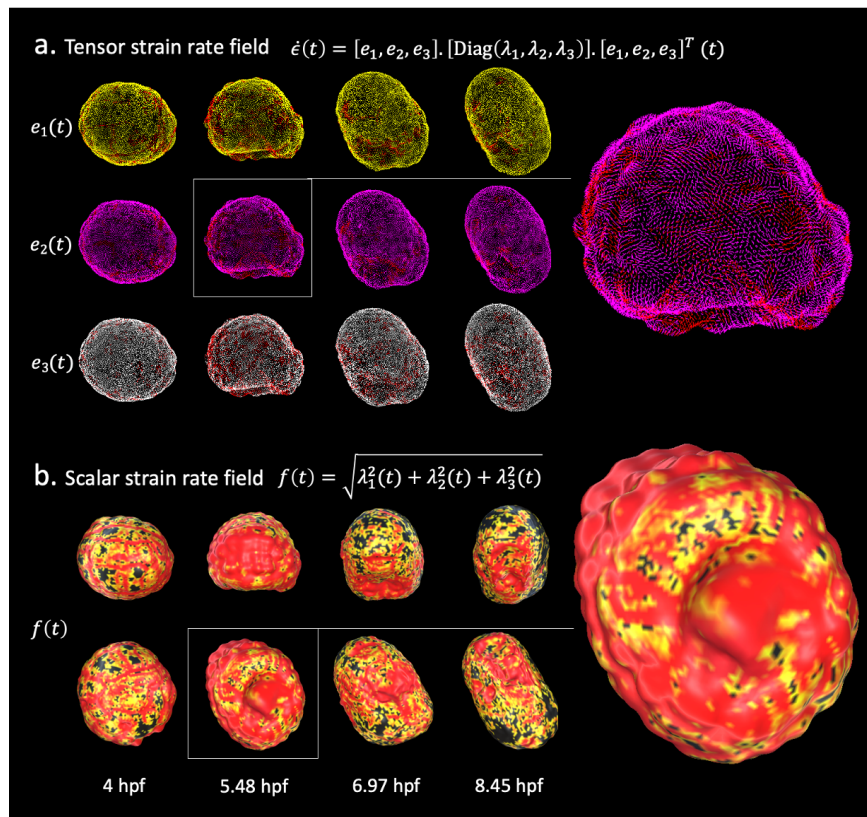


Figure 2. Strain-rate field describes morphogenesis. The strain-rate tensor field measures the rate at which morphological changes occur in the embryo as a function of time. The strain-rate tensor field is locally represented as a 3x3 symmetric matrix and is completely determined by its eigenvector fields. **a)** Heatmap of the eigenvector fields of the strain rate tensor. Each row represents a vector field distinguished by a distinct root color (yellow, pink, white). The gradient from the root color to red represents increasing levels of morphological activity. *Top* Spatiotemporal dynamics of the first eigenvector field. *Middle* Spatiotemporal dynamics of the second eigenvector field. *Bottom* Spatiotemporal dynamics of the third eigenvector field. **b)** Heatmap of the scalar strain rate field. The gradient from yellow to red depicts regions of increasing morphological activity, while black stands for areas of low morphological activity. The heatmaps show high morphological activity in the invaginating endoderm and zippering neural plate, but also across the embryonic animal during rounds of synchronized division.

198 Spherical harmonic basis functions are indexed by two parameters (l, m), such that $l \geq 0, |m| \leq l$
 199 representing respectively the degree and order of the harmonic (Supplementary figure 3). A signal
 200 defined on the sphere can be written as a linear combination of such functions. Decomposing a
 201 signal into spherical harmonics hence amounts to finding the coefficients f_{lm} of this weighted sum.
 202 In the case of our spatiotemporal scalar strain rate field, the coefficients f_{lm} are also a function of
 203 time and can be obtained as shown in equation 2.

$$f_{lm}(t) = \oint f(\theta, \phi, t) Y_{lm}^*(\theta, \phi) dA \quad (2)$$

204 Here, Y_{lm}^* stands for the complex conjugate of the spherical harmonic Y_{lm} . Moreover, for a given
 205 degree l , each of the $(2l + 1)$ spherical harmonics $(Y_{lm})_{|m| < l}$ spatially partitions the unit sphere into as
 206 many spatial domains indicating when a signal is positive, negative or null (Supp. Fig.4a). Figure 3a
 207 illustrate the projections of the scalar strain rate field to spherical harmonics $(Y_{lm})_{l \leq 2, |m| < l}$ at $t = 4.74$
 208 hpf, and their mapping unto the surface of the embryo. These plots reveal for instance that while
 209 there is no embryo-wide dominant morphogenesis process at this time ($l = 0, m = 0$), smaller
 210 regions, notably the vegetal pole are experiencing significant morphological activity ($l = 1, m = 0$).

211 The contributions of each spherical harmonic to the global signal can be assessed more rigorously, and interpreted in the light of biology. To this effect, we observe the temporal dynamics
212 of the coefficients $f_{lm}(t)$ associated with each spherical harmonic. In analogy to *Principal Components Analysis*, we measure the average variance ratio over time of each harmonic with respect
213 to the original signal (Fig. 3b). With a variance ratio of 64.4%, the spherical harmonic Y_{00} , capturing
214 embryo-wide morphological activity, contributes the most to ascidian morphogenesis. Spherical
215 harmonic Y_{10} is the next contributor, coming second with a variance ratio of 4.1%. This observation
216 is warranted, as Y_{10} maps to the animal and vegetal poles of the embryo, which are the epicenters
217 of synchronised cellular divisions and endoderm invagination respectively *Jeffery (1992); Lemaire (2009)*.
218 Interestingly, variances in the directions of Y_{00} and Y_{10} evolve in an antiphased pattern,
219 most notably in earlier parts of the plot, with Y_{00} contributing maximally (and Y_{10} minimally), during
220 periods of cell division, before relinquishing some variance shares to Y_{10} , which then peaks. This
221 suggests that while sporadic deformations induced by cellular divisions often dominate the landscape
222 of morphological activity, an observation consistent with studies in other species *Cislo et al. (2023)*,
223 other localised, slower processes are at play in the embryo. The described pattern tends to
224 fade out in the later parts of the plot, suggesting a shift in development dynamics.

225 Furthermore, by observing the time dynamics of the coefficients themselves (Fig. 3c), one can
226 easily identify which parts of the embryo are concerned by the morphological changes depicted.
227 For instance, the positive peaks in $f_{10}(t)$ (Fig. 3c) indicate that the morphological processes at hand
228 take place in the northern hemisphere of the sphere. Remarkably, these coincide with rapid growth
229 in cell population and thus synchronous cell divisions, which are known to be restricted to the
230 animal pole of the ascidian embryo during endoderm invagination *Jeffery (1992)*. In addition, most
231 of the dynamics captured by $f_{10}(t)$ are in the negative spectrum ($f_{10}(t) < 0$), pointing to the lower
232 hemisphere of the embryo, the foyer of several cell shape deformations at play in ascidian early
233 development.

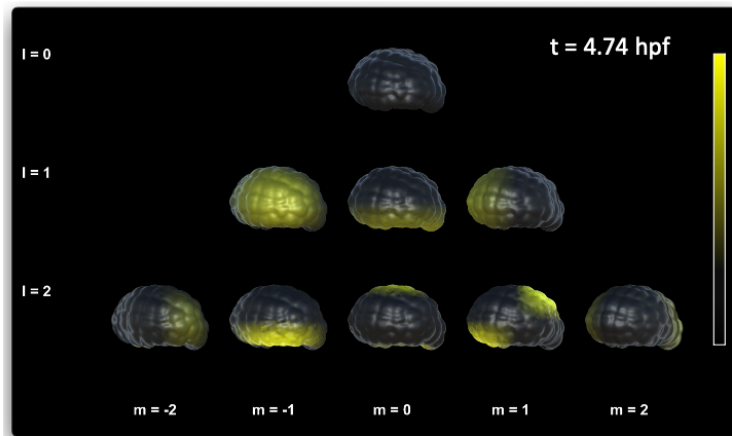
234 The sporadic short-time scale cell division events in the animal pole coexist with numerous
235 other features of morphogenesis, most notably, the larger scale continuous deformation process
236 in endoderm invagination at the embryonic vegetal pole. Beside the peaks on the plots of the time
237 series, it is not a trivial task to identify what other rich insights may be hidden in this data. A simple
238 observation of the oscillatory patterns of these main modes hence paints an incomplete picture
239 of ascidian morphogenesis. Extracting the footprint of all morphogenesis processes in these time
240 series requires further analysis.

243 **Spectral decomposition in time: Wavelets analysis of spherical harmonic signals unveils the blueprint of morphogenesis**

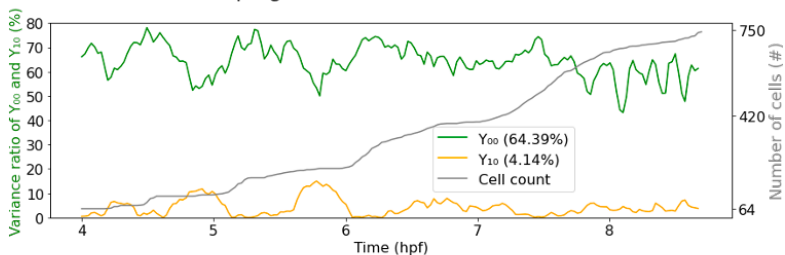
244 Analysing timeseries often implies the understanding of how a signal is composed and how its components
245 overlap in time. Wavelets have been put forward as effective multi-resolution tools able
246 to strike the right balance between resolution in time and resolution in frequency *Torrence and Compo (1998); Lau and Weng (1995)*. Although they have been taken advantage of in the broader
247 context of biology, most notably in the analysis of brain and heart signals *Brunton and Kutz (2022)*,
248 they have so far been under-used in developmental biology. The reason might be found in the
249 reality that morphogenesis data is often not understood in term of time series. Our spherical
250 harmonics decomposition of morphogenesis, inspired by similar endeavours in other fields *Dahlen and Tromp (2021); Knaack and Stenflo (2005)*, offers an unprecedented opportunity to leverage
251 the existing rich signal processing toolbox in development biology. In particular, enlisting the help
252 of wavelet transforms in unlocking the complex entanglements of the multiple morphological process
253 at play during ascidian early development. We proceed to apply the Ricker wavelet transform
254 to our spherical harmonics time series, normalised by mean and standard deviation in different
255 time windows of interest. The result is a set of spectrograms which decompose the signals into
256 canonical components organised in timelines that reveal the story ascidian morphogenesis.

257 First, we apply the wavelet transform on the timeseries $f_{00}(t)$ to the entire time range covered
258
259
260

a. Spherical harmonics decomposition of the strain rate eigen field



b. Dominant modes of morphogenesis



c. Timeseries of f_{00} and f_{10}

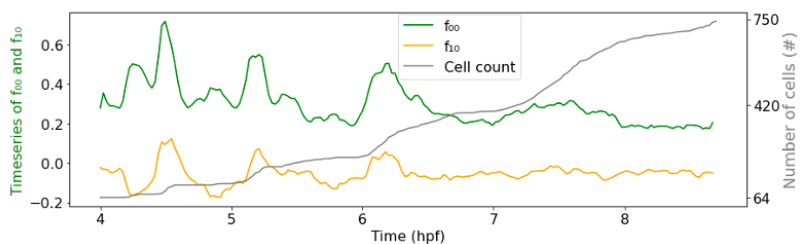


Figure 3. Spherical harmonics decomposition of morphogenesis. **a)** Example of Spherical harmonics decomposition of the scalar strain rate field mapped to the embryo at $t = 4.74$ hpf. **b)** Time evolution of the variance ratios of the main modes of ascidian early morphogenesis (Y_{00} and Y_{10}). The cell population dynamic is also included in the plot for clarity. **c)** Time evolution of the coefficients f_{00} and f_{10} associated with spherical harmonics (Y_{00} and Y_{10}). The cell population count is also included in the plot for clarity.

261 by our dataset, comprising both gastrulation and neurulation (fig. 4a). Mirroring this timeseries,
 262 the high frequency events depicted by yellow blobs at the top of the heatmap represent periods of
 263 synchronized division across the embryo. The dark band in the middle separating two large regions
 264 depicts a short transition phase delimiting two phases of ascidian early development. The timing
 265 of these stages as reflected in the scalogram matches the timeline of gastrulation and neurulation.
 266 Within both phases, the concentric gradients from red to yellow culminating in dense yellow spots
 267 in the center of both regions portray increasing morphodynamics.

268 To better understand the specifics of ascidian gastrulation, we restricted the wavelet transform
 269 to the gastrulation period ($t \in [4, 6.3]$ hpf). The resulting spectrogram (fig. 4b) shows that ascidian
 270 gastrulation unfolds itself in two major phases, delineated on the scalogram by the dark region at
 271 the center of the heatmap. The timeline of these events, strengthened by an analysis of topological
 272 holes in the embryo (supplementary fig. 4a) support the hypothesis that these phases correspond
 273 to endoderm invagination followed by the near-closing of the future gut, a process initiated by

274 the collective motion of lateral mesoderm cells known as *blastophore closure*. Both the timeseries
275 (mostly in the negative spectrum) and the scalogram of $f_{10}(t)$ (fig. 4c) adds another layer of validity
276 to this conclusion: the large yellow blob occupying the majority the plot surface highlights that fact
277 that regions of the embryo covered by spherical harmonic Y_{10} , hence endoderm and mesoderm
278 cells, are subject to intense and prolonged morphological processes.

279 The first of these two phases, namely endoderm invagination, has been thoroughly investigated
280 in literature. Most notably, it was identified that endoderm invagination was driven by two distinct
281 mechanisms of endoderm single cells *Sherrard et al. (2010)*: first, cells constricted apically by reduc-
282 ing the surface area of the apices, flattening the convex vegetal pole of the embryo setting the stage
283 for invagination. This was followed by animal vegetal shortening of their lateral faces, triggering
284 endoderm invagination. The wavelet transform restricted to the period of endoderm invagination
285 applied to $f_{20}(t)$, whose corresponding spherical harmonic function $Y_{20}(t)$ maps more precisely to
286 the endoderm, beautifully captures this two-steps process (fig. 4d). The timing revealed by this
287 scalogram is in accordance with an analysis endoderm cell shape ratios (supplementary fig. 4b).

288 **Spectral decomposition of morphogenesis in experimentally perturbed embryo**

289 To assess how our framework adapts to different phenotypes, we set out to conduct a spectral de-
290 composition of morphogenesis in an experimental manipulated embryo. In this particular mutant,
291 MEK kinase was inhibited, which resulted in a massive re-specification of vegetal cell fates, and
292 a disruption of endoderm invagination *Guignard et al. (2020)*. We applied to the mutant dataset
293 (fig 5a *top*) each of the steps in our workflow. First an evolving mesh matching the shape of the
294 embryo at every time point was obtained through the level set scheme. Then, a strain rate tensor
295 field was computed over the surface of the embryo throughout development time (fig 5a *bottom*).
296 A spatiotemporal spectral analysis was subsequently conducted using spherical harmonics on the
297 mutant surface and wavelet analysis of the timeseries of the coefficients of the main harmonic
298 modes. In order to meaningfully compare the dynamics of the mutant development against those
299 of the wild-type embryo, the analysis was carried out the 64-cell stage.

300 Similar to the wildtype (WT) embryo, the main harmonic modes in the mutant development
301 were Y_{00} and Y_{10} with respective variance ratios 73.68% and 1.65%, making the timeseries $f_{00}(t)$ and
302 $f_{10}(t)$ the main focus of our examination. The temporal dynamics of these coefficients already
303 reveal major differences between the two strains of ascidians (fig 5b). On the one hand, the drop
304 in the share of Y_{10} is telling of the lower order of morphological activity in the vegetal hemisphere.
305 The difference with WT embryos is even more striking when considering that they are deprived
306 of cell division in their vegetal hemisphere. On the other hand, the peaks and lows of $f_{10}(t)$ which
307 coincide with growth in cell numbers, are not restricted either to the negative or positive domain
308 of the curve. This implies that, contrary to the WT, synchronous cell divisions are not restricted to
309 one hemisphere of the embryo.

310 The wavelet transform applied to timeseries $f_{00}(t)$ and $f_{10}(t)$ yield spectrograms which bring fur-
311 ther insights into the mutant morphogenesis (fig 5c). On the one hand, the heatmap of $f_{00}(t)$ hints
312 to two distinct phases of the mutant development during the observed time span (fig 5c *top*). The
313 timing of the second phase seems to coincide with the advent of the major wave of cell divisions
314 in the embryo. On the other hand, plots of the scalogram of $f_{10}(t)$ appears to concur with the hy-
315 pothesis of very low morphological activity in the vegetal pole. The constant red on this heatmap
316 reflects unchanging levels of morphological activity at the vegetal pole of the embryo and confirms
317 the absence of drastic cell deformations that usually drive invagination. This is in alignment with
318 the perturbation induced by MEK kinase which prevents invagination for happening in the mutant
319 endoderm.

320 **Discussion**

321 Ray Keller's roadmap of morphogenesis studies establishes a clear path for understanding the
322 biomechanical processes involved in development *Keller et al. (2003)*. In his proposed workflow,

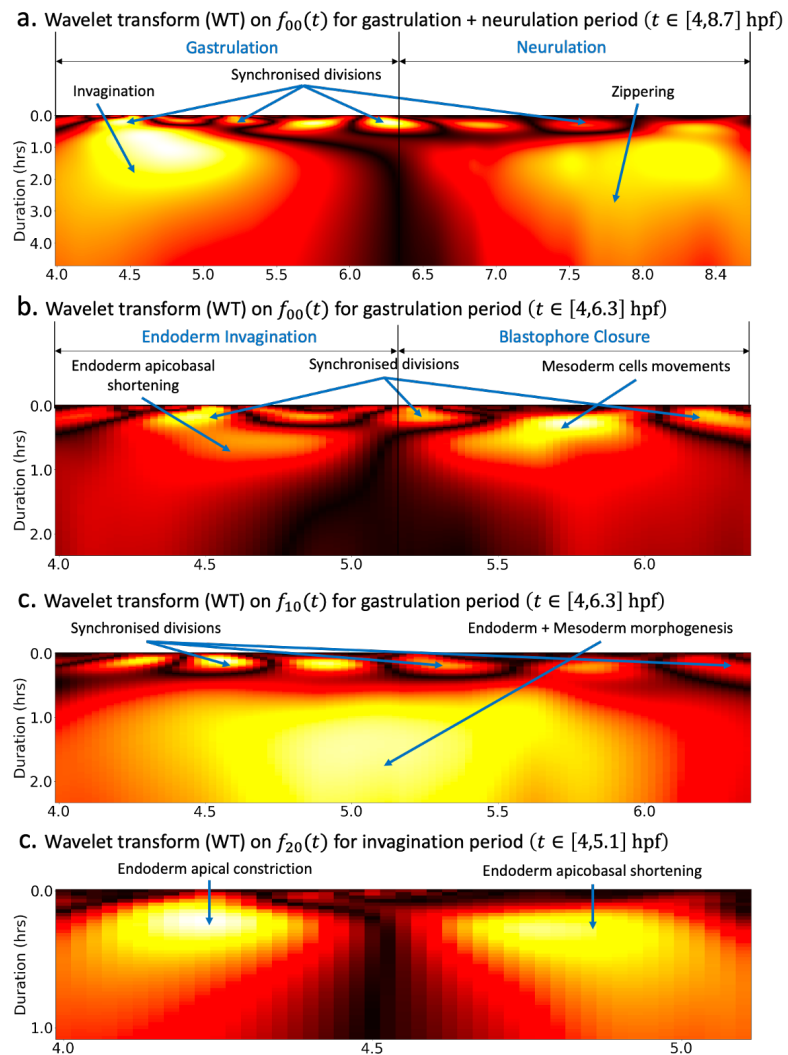
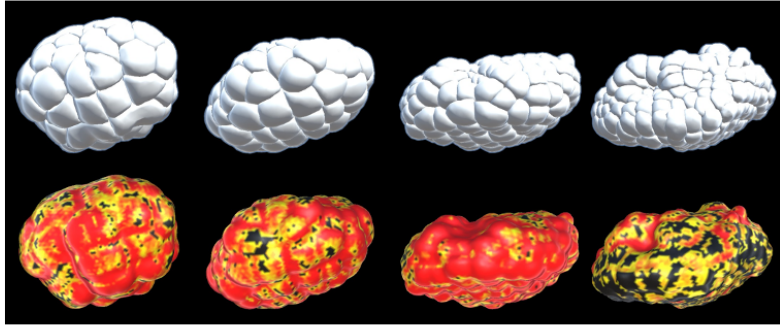


Figure 4. Wavelet analysis highlights multi-timescale modes of morphogenesis. **a)** Scalogram resulting from the ricker wavelet transform applied to $f_{00}(t)$ over the whole period covered by the dataset $t \in [4, 8.6]$ hpf. **b)** Scalogram resulting from the ricker wavelet transform applied to $f_{00}(t)$ restricted to the gastrulation period $t \in [4, 6.3]$ hpf. The high frequency events highlighted here represent time points of synchronized division across the embryo. The dark band in the middle separating two large red regions indicates that there are two phases of invagination characterized by large deformations and a relatively calm transition phase in between. **c)** Scalogram resulting from the ricker wavelet transform applied to $f_{10}(t)$ restricted to the gastrulation period $t \in [4, 6.3]$ hpf. Similar to **b)**, the high frequency events indicate synchronized division in the embryo. **d)** Scalogram resulting from the ricker wavelet transform applied to $f_{20}(t)$ restricted to endoderm invagination $t \in [4, 5.1]$ hpf.

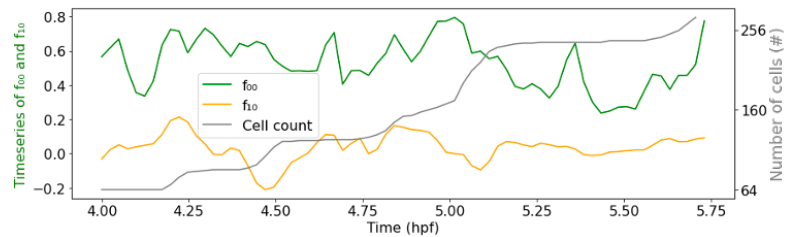
323 the first step is to determine when and where cells move. Identifying regions of significant mor-
 324 phological activity in space and time has usually followed a script consisting of observing via a mi-
 325 croscope the developing system, formulating a hypothesis of what is happening in the system, and
 326 subsequently affirming or refuting the hypothesis using qualitative analysis. This method, which
 327 has successfully propelled the field of developmental biology to its current heights, nevertheless
 328 has some limitations. Distinct morphogenesis events can overlap both in space and time, render-
 329 ing eye observation vulnerable to misinterpretation. Second, these methods are not automated,
 330 hence do not scale.

331 In this work, we attempted to develop an alternative approach to probing development in liv-

a. Ascidian mutant morphogenesis + strain rate mapped to the surface of the mutant



b. Timeseries of f_{00} and f_{10}



c. Wavelet transform on $f_{00}(t)$ and $f_{10}(t)$ for Mutant embryo

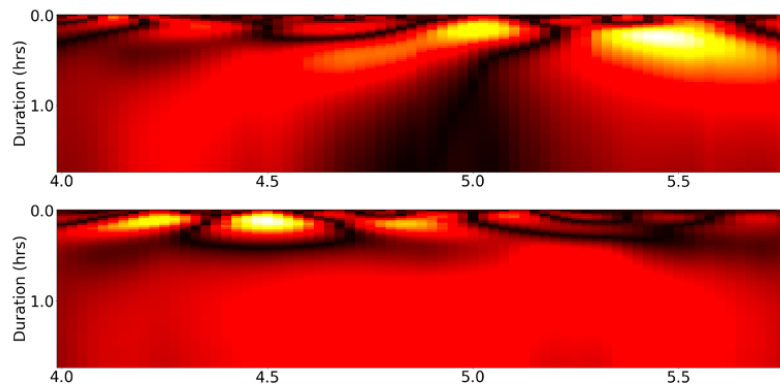


Figure 5. Spectral decomposition of morphogenesis in mutant embryo. a) *Top* Ascidian mutant morphogenesis. *Bottom* Spatiotemporal scalar strain rate field mapped to the mutant surface. **b)** Time evolution of the coefficients f_{00} and f_{10} associated with spherical harmonics (Y_{00} and Y_{10}). The cell population dynamic is also included in the plot for clarity. **c)** Wavelet transform applied on $f_{00}(t)$ (*top*) and $f_{10}(t)$ (*bottom*).

332 ing systems. Our approach takes advantage of the recent boom in the availability of single cell
 333 shape tracking data to propose a generic method able to identify interesting defining morpholog-
 334 ical processes through space and time in developing embryos. The method takes as input data
 335 consisting of evolving cell geometries and outputs a series of spatial heatmaps showcasing in the
 336 time-frequency domains the most salient traits of morphogenesis in the studied embryo. There is
 337 however no requirement for segmented cells: the method can be extended to accommodate mi-
 338 croscopy imaging data. Our framework presents over the traditional eye test method multiple ad-
 339 vantages. First, the workflow is fully automated, providing an unprecedented hands-off approach
 340 in preliminary studies of morphogenesis. Another outstanding advantage over traditional is that
 341 our workflow is able to compress the story of the development, such that, in a single image, one can
 342 grasp the essence of morphogenesis in a system of interest. In particular, our method has been
 343 able to neatly discriminate between the gastrulation and neurulation phases of ascidian early de-
 344 velopment, identify a second phase of gastrulation: *blastophore closure* which follows invagination,
 345 reconstitute the two-step process of endoderm invagination during the gastrulation phase, while

346 clearly distinguishing between short scale division events and low frequency tissue-wide deforma-
347 tions.

348 In order to achieve this fit, raw cell shape data underwent a series of transformations includ-
349 ing a level-sets driven homeomorphic map of the unit sphere to the developing embryo's surface,
350 the computation of the strain rate field of embryo deformations through time using successive
351 iterations of this map, a spherical harmonics decomposition of this strain-rate field, and wavelet
352 decomposition of the most significant spherical harmonics time series. Each of these transfor-
353 mations comes with its own challenges, but also delivers new perspectives for the study of living
354 systems. Our level set scheme excels at defining a homeomorphic map between the unit sphere
355 and surface of the embryo. It goes without saying that in order for the deformed sphere to best
356 match the shape of the embryo, a high sampling of points on the unit sphere is required. A com-
357 promise is however necessary between this sampling and, on the one hand, the overall spatial
358 resolution of the raw data, on the other hand, the induced computational complexity. In its cur-
359 rent form, the scheme produces approximations of Lagrangian particles only under the assumption
360 of small deformations in the embryo. Hence, the sampling rate during microscopy imaging is of
361 critical importance: the shorter intervals between two successive frames of the movie, the more
362 Lagrangian-like the particles are expected to behave.

363 Given the provision of tracked surface particles meshed at every frame in a triangular network,
364 the evaluation of the strain rate field is straightforward, and enables, among others, a unified de-
365 scription of complex cell-level and tissue-level dynamics *Blanchard et al. (2009)*, such as drastic
366 deformations and synchronised divisions. The accuracy of this field is affected, as previously, by
367 both the spatial sampling of material points on the unit sphere and the timely sampling of morpho-
368 genesis frames. A visualisation of the eigenvalue field derived from this tensor field on the surface
369 of the embryo can already highlight significant processes in morphogenesis. The decomposition of
370 this field into spherical harmonics allows a better appreciation of the spatial patterns of morpho-
371 logical activity in the embryo, each harmonic mapping a region of space. Our spherical harmonics
372 decomposition of morphogenesis results in a set of timeseries of coefficients associated with each
373 harmonic, representing, to the best of our acknowledge, the first comprehensive timeseries-based
374 description of morphogenesis. This transformation unleashes the full power of signal processing
375 tools into studies of morphogenesis. The basis of spherical harmonics being infinite, a challenge
376 here is to discriminate between harmonics that significantly contribute to the composed signal
377 and those that do not. Here, this was done by singling-out harmonics which contributed the most
378 to the variance of the strain rate field. Furthermore, the filtration of principal harmonics modes
379 enables the representation of morphogenesis in a significantly compressed form, in comparison
380 to the initial datasets. This lower dimensional representation of morphogenesis can be helpful,
381 among others, in modelling the physical dynamics of the system *Romeo et al. (2021)*. Another chal-
382 lenge is with the interpretability of the harmonics, which is subject to the alignment of the embryos.
383 The datasets used in this paper presented the advantage that their y - axis was quasi-aligned with
384 their *vegetal* - *animal* axis. For embryos which do not have this property, prior processing to align
385 them will be required. Alternatively, rotation-invariant representations can be used to appropri-
386 ately interpret the harmonics.

387 Despite describing canonical interactions in the space of spherical harmonic functions, our
388 spherical timeseries still represent composed signals in time. We use the *Ricker Wavelet* as a math-
389 ematical microscope to zoom-in and zoom-out through these signals in order to identify their fun-
390 damentals components. This operation results in two-dimensional time-frequency heatmaps that
391 showcase, for each time-series, the footprint of its canonical high and low frequency components,
392 which can be mapped to biological processes. The sum of these tell the story of morphogenesis
393 in the region corresponding to the spherical harmonic. Here, it might also be useful to wisely tar-
394 get windows of time of interest, and to normalise the data such that interesting transitions can be
395 picked up easily by the wavelet transforms. The resulting heatmaps can be fed to analytic work-
396 flows such as deep neural networks for further studies. Example scenarios could include varia-

397 tional studies of morphogenesis processes in different wild-type or mutant embryo. Furthermore,
398 the workflow presented in this paper can be applied to the examination of single cell morphological
399 behaviours in development.

400 References

- 401 **Alba V**, Carthew JE, Carthew RW, Mani M. Global constraints within the developmental program of the
402 *Drosophila* wing. *Elife*. 2021; 10:e66750.
- 403 **Ambrosi D**, Ateshian GA, Arruda EM, Cowin S, Dumais J, Goriely A, Holzapfel GA, Humphrey JD, Kemkemer R,
404 Kuhl E, et al. Perspectives on biological growth and remodeling. *Journal of the Mechanics and Physics of*
405 *Solids*. 2011; 59(4):863–883.
- 406 **Bar-Kochba E**, Toyjanova J, Andrews E, Kim KS, Franck C. A fast iterative digital volume correlation algorithm
407 for large deformations. *Experimental Mechanics*. 2015; 55(1):261–274.
- 408 **Blanchard GB**, Kabla AJ, Schultz NL, Butler LC, Sanson B, Gorfinkiel N, Mahadevan L, Adams RJ. Tissue tectonics:
409 morphogenetic strain rates, cell shape change and intercalation. *Nature methods*. 2009; 6(6):458–464.
- 410 **Brunton SL**, Kutz JN. *Data-driven science and engineering: Machine learning, dynamical systems, and control*.
411 Cambridge University Press; 2022.
- 412 **Cislo DJ**, Yang F, Qin H, Pavlopoulos A, Bowick MJ, Streichan SJ. Active cell divisions generate fourfold orienta-
413 tionally ordered phase in living tissue. *Nature Physics*. 2023; p. 1–10.
- 414 **Dahlen F**, Tromp J. Theoretical global seismology. In: *Theoretical Global Seismology* Princeton university press;
415 2021.
- 416 **Dalmaso G**, Musy M, Niksic M, Robert-Moreno A, Badía-Careaga C, Sanz-Ezquerro JJ, Sharpe J. 4D reconstruc-
417 tion of developmental trajectories using spherical harmonics. *bioRxiv*. 2021; .
- 418 **De Goes F**, Butts A, Desbrun M. Discrete differential operators on polygonal meshes. *ACM Transactions on*
419 *Graphics (TOG)*. 2020; 39(4):110–1.
- 420 **Dokmegang J**. Modeling Epiblast Shape in Implanting Mammalian Embryos. In: *Epiblast Stem Cells* Springer;
421 2022.p. 281–296.
- 422 **Dokmegang J**, Yap MH, Han L, Cavaliere M, Doursat R. Computational modelling unveils how epiblast remod-
423 elling and positioning rely on trophectoderm morphogenesis during mouse implantation. *Plos one*. 2021;
424 16(7):e0254763.
- 425 **Godard BG**, Heisenberg CP. Cell division and tissue mechanics. *Current opinion in cell biology*. 2019; 60:114–
426 120.
- 427 **Guignard L**, Fiúza UM, Leggio B, Laussu J, Faure E, Michelin G, Biasuz K, Hufnagel L, Malandain G, Godin C, et al.
428 Contact area-dependent cell communication and the morphological invariance of ascidian embryogenesis.
429 *Science*. 2020; 369(6500).
- 430 **Hardy A**, Steeb WH. *Mathematical Tools in Computer Graphics with C# Implementations*. WORLD SCIENTIFIC;
431 2008. <https://www.worldscientific.com/worldscibooks/10.1142/6725>, doi: 10.1142/6725.
- 432 **Hashimoto H**, Munro E. Dynamic interplay of cell fate, polarity and force generation in ascidian embryos.
433 *Current opinion in genetics & development*. 2018; 51:67–77.
- 434 **Hashimoto H**, Robin FB, Sherrard KM, Munro EM. Sequential contraction and exchange of apical junctions
435 drives zippering and neural tube closure in a simple chordate. *Developmental cell*. 2015; 32(2):241–255.
- 436 **Humphrey JD**. Continuum biomechanics of soft biological tissues. *Proceedings of the Royal Society of London*
437 *Series A: Mathematical, Physical and Engineering Sciences*. 2003; 459(2029):3–46.
- 438 **Humphrey JD**. *Cardiovascular solid mechanics: cells, tissues, and organs*. Springer Science & Business Media;
439 2013.
- 440 **Jeffery WR**. A gastrulation center in the ascidian egg. . 1992; .
- 441 **Jones RA**, Renshaw MJ, Barry DJ, Smith JC. Automated staging of zebrafish embryos using machine learning.
442 *Wellcome Open Research*. 2022; 7(275):275.

- 443 **Keller R**, Davidson LA, Shook DR. How we are shaped: the biomechanics of gastrulation. *Differentiation:*
444 ORIGINAL ARTICLE. 2003; 71(3):171–205.
- 445 **Knaack R**, Stenflo JO. Spherical harmonic decomposition of solar magnetic fields. *Astronomy & Astrophysics.*
446 2005; 438(1):349–363.
- 447 **Lau KM**, Weng H. Climate signal detection using wavelet transform: How to make a time series sing. *Bulletin*
448 *of the American meteorological society.* 1995; 76(12):2391–2402.
- 449 **Leggio B**, Laussu J, Carlier A, Godin C, Lemaire P, Faure E. MorphoNet: an interactive online morphological
450 browser to explore complex multi-scale data. *Nature communications.* 2019; 10(1):1–8.
- 451 **Lemaire P**. Unfolding a chordate developmental program, one cell at a time: invariant cell lineages, short-range
452 inductions and evolutionary plasticity in ascidians. *Developmental biology.* 2009; 332(1):48–60.
- 453 **Mancinelli C**, Livesu M, Puppo E. Gradient Field Estimation on Triangle Meshes. In: *STAG*; 2018. p. 87–96.
- 454 **Michelin G**, Guignard L, Fiuza UM, Lemaire P, Godine C, Malandain G. Cell pairings for ascidian embryo regis-
455 tration. In: *2015 IEEE 12th International Symposium on Biomedical Imaging (ISBI)* IEEE; 2015. p. 298–301.
- 456 **Mitchell NP**, Lefebvre MF, Jain-Sharma V, Claussen N, Raich MK, Gustafson HJ, Bausch AR, Streichan SJ. Mor-
457 phodynamic Atlas for Drosophila Development. *bioRxiv.* 2022; p. 2022–05.
- 458 **Mitchell NP**, Cislo DJ. TubULAR: Tracking deformations of dynamic tissues and interfaces in 3D. *bioRxiv.* 2022;
459 .
- 460 **Nishida H**. Cell Division Pattern during Gastrulation of the Ascidian, *Halocynthia roretzi*: (cell division pat-
461 tern/gastrulation/neurulation/ascidian embryo). *Development, growth & differentiation.* 1986; 28(2):191–
462 201.
- 463 **Patel M**, Leggett SE, Landauer AK, Wong IY, Franck C. Rapid, topology-based particle tracking for high-resolution
464 measurements of large complex 3D motion fields. *Scientific reports.* 2018; 8(1):1–14.
- 465 **Power RM**, Huiskens J. A guide to light-sheet fluorescence microscopy for multiscale imaging. *Nature methods.*
466 2017; 14(4):360–373.
- 467 **Romeo N**, Hastewell A, Mietke A, Dunkel J. Learning developmental mode dynamics from single-cell trajectories.
468 *Elife.* 2021; 10:e68679.
- 469 **Satoh N**. Cellular morphology and architecture during early morphogenesis of the ascidian egg: an SEM study.
470 *The Biological Bulletin.* 1978; 155(3):608–614.
- 471 **Sherrard K**, Robin F, Lemaire P, Munro E. Sequential activation of apical and basolateral contractility drives
472 ascidian endoderm invagination. *Current Biology.* 2010; 20(17):1499–1510.
- 473 **Stegmaier J**, Amat F, Lemon WC, McDole K, Wan Y, Teodoro G, Mikut R, Keller PJ. Real-time three-dimensional
474 cell segmentation in large-scale microscopy data of developing embryos. *Developmental cell.* 2016;
475 36(2):225–240.
- 476 **Stelzer EH**. Light-sheet fluorescence microscopy for quantitative biology. *Nature methods.* 2015; 12(1):23–26.
- 477 **Stout DA**, Bar-Kochba E, Estrada JB, Toyjanova J, Kesari H, Reichner JS, Franck C. Mean deformation metrics
478 for quantifying 3D cell–matrix interactions without requiring information about matrix material properties.
479 *Proceedings of the National Academy of Sciences.* 2016; 113(11):2898–2903.
- 480 **Streichan SJ**, Lefebvre MF, Noll N, Wieschaus EF, Shraiman BI. Global morphogenetic flow is accurately pre-
481 dicted by the spatial distribution of myosin motors. *Elife.* 2018; 7:e27454.
- 482 **Tassy O**, Daian F, Hudson C, Bertrand V, Lemaire P. A quantitative approach to the study of cell shapes and
483 interactions during early chordate embryogenesis. *Current Biology.* 2006; 16(4):345–358.
- 484 **Torrence C**, Compo GP. A practical guide to wavelet analysis. *Bulletin of the American Meteorological society.*
485 1998; 79(1):61–78.
- 486 **Zhao HK**, Osher S, Merriman B, Kang M. Implicit and nonparametric shape reconstruction from unorganized
487 data using a variational level set method. *Computer Vision and Image Understanding.* 2000; 80(3):295–314.